Materials Science and Engineering B 185 (2014) 123–128

Contents lists available at ScienceDirect

Materials Science and Engineering B

journal homepage: www.elsevier.com/locate/mseb

Short communication

Investigation of the structural, optical and dielectric properties of highly (1 0 0)-oriented $(Pb_{0.60}Ca_{0.20}Sr_{0.20})TiO_3$ thin films on $LaNiO_3$ bottom electrode

D.S.L. Pontes [a], F.M. Pontes [b,*], A.J. Chiquito [c], E. Longo [a,d]

[a] Laboratorio Interdisciplinar de Eletroquimica e Cerâmica, Department of Chemistry, Universidade Federal de São Carlos, Via Washington Luiz, Km 235, P.O. Box 676, 13565-905 São Carlos, São Paulo, Brazil
[b] Department of Chemistry, Universidade Estadual Paulista, P.O. Box 473, 17033-360 Bauru, São Paulo, Brazil
[c] NanO LaB, Transporte Eletrônico em Nanoestruturas, Department of Physics, Universidade Federal de São Carlos, Via Washington Luiz, Km 235, P.O. Box 676, 13565-905 São Carlos, São Paulo, Brazil
[d] Institute of Chemistry, Universidade Estadual Paulista, Araraquara, São Paulo, Brazil

ARTICLE INFO

Article history:
Received 31 October 2013
Received in revised form 4 February 2014
Accepted 23 February 2014
Available online 7 March 2014

Keywords:
Thin films
Chemical synthesis
Optical properties
Ferroelectric properties

ABSTRACT

Highly (1 0 0)-oriented $Pb_{0.60}Ca_{0.20}Sr_{0.20}TiO_3$/LNO/LAO structure was fabricated using a chemical deposition process via spin-coating technique. XRD revealed that both LNO and $Pb_{0.60}Ca_{0.20}Sr_{0.20}TiO_3$ films grown on LAO(1 0 0) substrate and LNO/LAO(1 0 0) structure were crystallized to be highly (*h* 0 0)-oriented, respectively. AFM images revealed smooth surfaces, spherical-shaped grains and a crack-free surface with a roughness of about 3–7 nm. The tetragonal perovskite phase was confirmed by Raman spectroscopy for $Pb_{0.60}Ca_{0.20}Sr_{0.20}TiO_3$/LNO/LAO and $Pb_{0.60}Ca_{0.20}Sr_{0.20}TiO_3$/LAO structures. The optical transmittance of 340 nm thick $Pb_{0.60}Ca_{0.20}Sr_{0.20}TiO_3$ films on a LAO(1 0 0) substrate exhibited an average transmittance above 80% in the wavelength range of 500–1000 nm and an optical band gap E_g of 3.56 and 2.87 eV for the direct and indirect transition processes, respectively. The Au/$Pb_{0.60}Ca_{0.20}Sr_{0.20}TiO_3$/LNO/LAO structure has a hysteresis loop with remnant polarization, P_r, of 12 μC/cm^2, and a coercive field, E_c, of 46 kV/cm for an electric field at 370 kV/cm along with a dielectric constant over 1200.

1. Introduction

Ferroelectric perovskite thin films had a rapid progress in recent years for their potential applications in ultrahigh density memory devices, tunable microwave devices, infrared, humidity and gas sensors, photochemical water oxidation devices, etc. [1–3]. Several literature reports have been published on the improvement of dielectric properties and the production of high performance ferroelectric thin films by studying the influence of: (1) preparation conditions; (2) use of a single crystal substrate; (3) orientation; and (4) the effect of conductive metallic oxide electrodes (*CMOEs*) on physical and chemical properties of ferroelectric thin films [4–6].

CMOEs significantly affect ferroelectric, piezoelectric and dielectric properties of perovskite thin films. In this context, one particular approach is dedicated to conductive metallic oxide films such as $LaNiO_3$, $SrRuO_3$, $BaPbO_3$ and $La_{1-x}Sr_xCoO_3$ [7–10]. These oxides were used to replace the Pt bottom electrode that usually causes serious fatigue problems mainly on $PbTiO_3$ and $Pb(Zr,Ti)O_3$ thin films [11,12]. Among these *CMOEs*, $LaNiO_3$ has been the most widely investigated. In addition, it exhibits a pseudocubic perovskite structure with a small degree of rhombohedral distortion as well as a relatively simple composition. Its crystallographic compatibility with the major perovskite structure of ferroelectric thin films is considerably beneficial to obtain highly oriented, texturized or epitaxial $LaNiO_3$ thin films for use in different device architectures which favor rapid integration into electro-electronic devices [13,14]. $LaNiO_3$ films were prepared by a number of methods, including chemical solution method, sputtering, molecular beam epitaxy and pulsed laser deposition [15–19]. At the same time, epitaxial, textured or highly oriented ferroelectric thin films has successfully produced with better properties than polycrystalline films. Recently, Han et al. [17] reported high-quality Pt/LNO/PZT/LNO/Pt multilayer architecture using the chemical solution deposition method. The Pt/LNO/PZT/LNO/Pt multilayer architecture exhibited excellent ferroelectric and dielectric properties.

* Corresponding author. Tel.: +55 14 3103 6135; fax: +55 14 3103 6088.
E-mail address: fenelon@fc.unesp.br (F.M. Pontes).

http://dx.doi.org/10.1016/j.mseb.2014.02.020
0921-5107/

Researchers reported that the formation of the pyrochlore deleterious phase could be effectively suppressed by the insertion of an adequate conductive metallic oxide electrode deposited onto platinum-coated silicon substrates [20–22]. However, a number of studies where ferroelectric thin films were grown on Pt electrodes showed that these samples contained considerable amount of the pyrochlore phase that was deleterious to electrical properties; i.e., lower dielectric constant and remnant polarization values. Takahara et al. [21] reported that PZT thin films deposited directly on a platinum-coated MgO single crystal substrate by a pulsed laser deposition (PLD) technique resulted in the predominant pyrochlore phase.

In this study, both $LaNiO_3$ and (Ca,Sr) A-site co-substituted $PbTiO_3$ thin films highly (1 0 0)-oriented were fabricated by the chemical solution deposition method on $LaAlO_3$ (1 0 0) single crystal substrate. We also reported the crystal structure, microstructure, optical and ferroelectric properties of $(Pb,Ca,Sr)TiO_3$ complex perovskite thin films grown on $LaNiO_3$(1 0 0)/$LaAlO_3$(1 0 0) and $LaAlO_3$(1 0 0).

2. Experimental procedures

Our procedure for synthesizing $Pb_{0.60}Ca_{0.20}Sr_{0.20}TiO_3$ and $LaNiO_3$ (PCST60 and LNO, respectively) thin films facilitated the use of a chemical solution deposition method (the polymeric precursor route). Details of the preparation method can be found in the literature [23].

First, $LaNiO_3$ thin films were spin coated on (1 0 0)$LaAlO_3$ single crystal substrates (LAO) by a spin coater (KW-4B, Chemat Technology) operating at 7200 revolutions/min for 30 s. Each annealing layer was placed on a hot plate preheated to 150 °C for 5 min for drying and then prefired at 400 °C for 4 h at a heating rate of 5 °C/min in a tube oven in an oxygen atmosphere to pyrolyze the organic materials followed by heating at 700 °C for 2 h at a heating rate of 5 °C/min for crystallization in an oxygen atmosphere. The film thickness was controlled by adjusting the number of coatings and the rotation. Each layer was pyrolyzed at 400 °C and crystallized at 700 °C before the next layer was deposited. These coating/drying operations were repeated until the desired thickness was obtained. Second, the PCST60 thin films were deposited by spinning the precursor solution by a spin coater (KW-4B, Chemat Technology) operating at 7200 revolutions/min for 30 s for the $LaNiO_3/LaAlO_3$ multilayer architecture. In this case, PCST60 thin films were annealed at 400 °C for 4 h and then at 650 °C for 2 h in a tube oven in an oxygen atmosphere. Through this process, thickness values of about 360 nm for LNO and 260 nm for PCST60 were obtained by repeating the spin-coating and heating treatment cycles.

Following the procedure described above, we spin-coated thin films of PCST60 on a (1 0 0)$LaAlO_3$ single crystal substrate for optical transmittance characterization.

Structural features of these thin films were characterized by XRD measurements which were performed in all samples by using Cu-Kα radiation on a Rigaku D/Max-2400 diffractometer. Typical 2θ angular scans ranging from 20 to 60° with an interval of 0.02° and scanning rate of 2°/min were used in these experiments. Changes in the morphology of the PCST60/$LaNiO_3$/$LaAlO_3$ multilayer architecture were analyzed by AFM. These images were analyzed using Digital Instruments Multimode Nanoscope IIIa (Santa Barbara, CA) software. The film thickness was evaluated by observing film cross-sections using field emission-scanning electron microscopy (FE-SEM) (FEG-VP Zeiss Supra 35) with a secondary electron detector on a freshly fractured film/substrate cross-section. Unpolarized Raman spectroscopy measurements were taken at room temperature with a T-64000 Jobin-Yvon triple-monochromator coupled to a charge-coupled detector (CCD). An optical microscope with a 100× objective was used to focus the 514.5 nm line of a Coherent Innova 70 argon laser onto the sample. The laser output power was maintained at about 15 mW. The PCST60 thin film optical transmittance on a (1 0 0)$LaAlO_3$ single crystal substrate annealed at 650 °C was measured in the wavelength range of 200–1000 nm using a Shimadzu 1240 spectrophotometer.

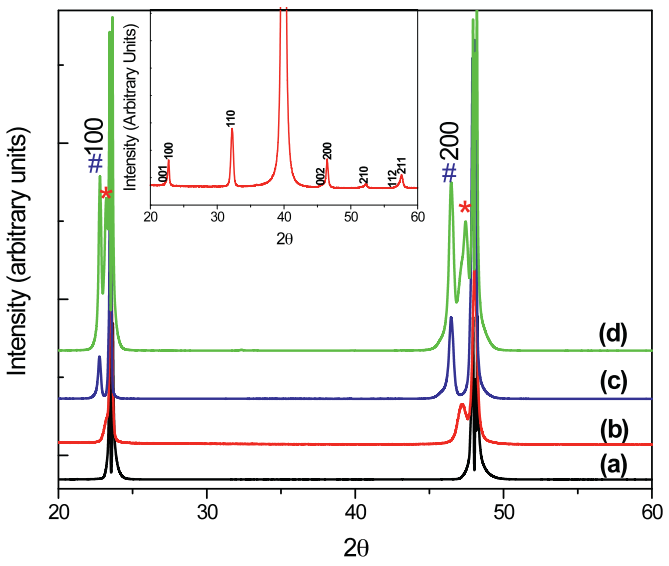

Fig. 1. XRD patterns: (a) the pure $LaAlO_3$(100) single crystal substrate; (b) a $LaNiO_3$ thin film on a $LaAlO_3$(100) single crystal substrate; (c) a PCST60 thin film on a $LaAlO_3$(1 0 0) single crystal substrate; and (d) a PCST60/$LaNiO_3$/$LaAlO_3$ multilayer structure. The inset shows the XRD patterns of the polycrystalline PCST60 thin films on $Si/SiO_2/Ti/Pt$ substrate. #, Thin film; *, $LaNiO_3$; X, substrate.

For electrical property measurements, circular Au electrodes were prepared by evaporation through a shadow mask with a 4.9×10^{-2} mm^2 dot area to obtain an array of capacitors. The deposition was carried out under vacuum (10^{-5} Torr). The polarization hysteresis nature of the film was analyzed using a ferroelectric tester system (Premier Precision from Radiant Technologies, Inc.). The dielectric constant frequency dependence and the dielectric loss were measured by an Agilent 4294A Precision Impedance Analyzer in the frequency region of 100 Hz–1 MHz. The capacitance–voltage (C–V) curves were measured using an Agilent 4294A Precision Impedance Analyzer with an AC signal of 50 mV at 100 kHz. All measurements were conducted at room temperature. In addition, phase transition study was accomplishment by electrical measurements. Temperature-dependent dielectric constants were studied in a Au/PCST60/LNO/LAO sandwich structural configuration, and the films were characterized using a G^w Instek LCR 819 meter at temperatures ranging from 300 to 523 K.

3. Results and discussion

Fig. 1 shows XRD patterns for pure LAO(1 0 0) single crystal substrate, LNO/LAO and PCST60/LNO/LAO architecture. In addition, LAO(1 0 0) single crystal substrate structure differs from the cubic perovskite only by small antiphase rotations of AlO_6 octahedra which are pseudocubic with a lattice parameter of 0.3791 nm [24]. The reasonably small lattice mismatch of LNO and a relatively small difference in thermal expansion coefficients between LNO and LAO are often adequate for highly preferential growth of LNO films on LAO substrate [25]. XRD patterns for LNO/LAO structures show only strong reflections from LNO(h 0 0) diffraction planes and were indexed according to a pseudocubic structure into the perovskite single phase with no trace of any impurity peaks (see Fig. 1(b)) which demonstrates the highly oriented growth of the conductive

metallic oxide film on LAO(1 0 0) single crystal substrate. The LNO conductive metallic oxide perovskite structure had a lattice constant of 0.3850 nm. Fig. 1(c) shows the PCST60 films were deposited directly onto the LAO(1 0 0) single crystal substrate which also shows highly (*h* 0 0)-oriented growth. The strong (*h* 0 0)-orientation of the PCST60/LAO structure is due to factors mentioned below. PCST60 films were then deposited on the LNO/LAO multilayer structure, Fig. 1(d). PCST60 thin film deposited on the LNO/LAO multilayer structure also demonstrates a well developed perovskite phase without other crystalline phases with stronger preferred (*h* 0 0) orientation due to the similar crystal structure as well as good matching of the lattice parameters (in-plane) between the LNO oxide film and PCST60 thin films (0.3850 nm and 0.3906 nm, respectively). Lattice mismatch values for LNO/LAO, PCST60/LAO and PCST60/LNO/LAO architectures are 1.56%, 2.76% and 1.45%, respectively. Low values for lattice mismatches obtained for PCST60 films deposited on both LNO and LAO exhibit very good orientation (see XRD figure for (*h* 0 0) reflection in Fig. 1). The inset in Fig. 1 shows the X-ray diffraction patterns for the polycrystalline PCST60 thin films grown on $Si/SiO_2/Ti/Pt$ substrate.

Micro-Raman spectroscopy was used for the structural study. Fig. 2(a) and (b) shows unpolarized Raman spectra recorded at 300 K of PCST60 thin film deposited directly on LAO(1 0 0) single crystal substrate and of PCST60 film deposited on LNO/LAO multilayer structure, respectively. In addition, Raman features related to the PCST60 thin film deposited directly on LAO(1 0 0) single crystal

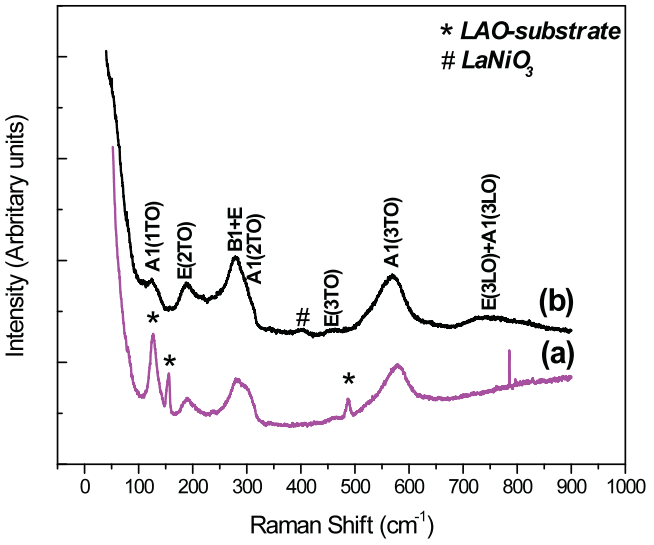

Fig. 2. Room temperature unpolarized micro-Raman spectra: (a) PCST60/LAO; and (b) a PCST60/LNO/LAO multilayer structure.

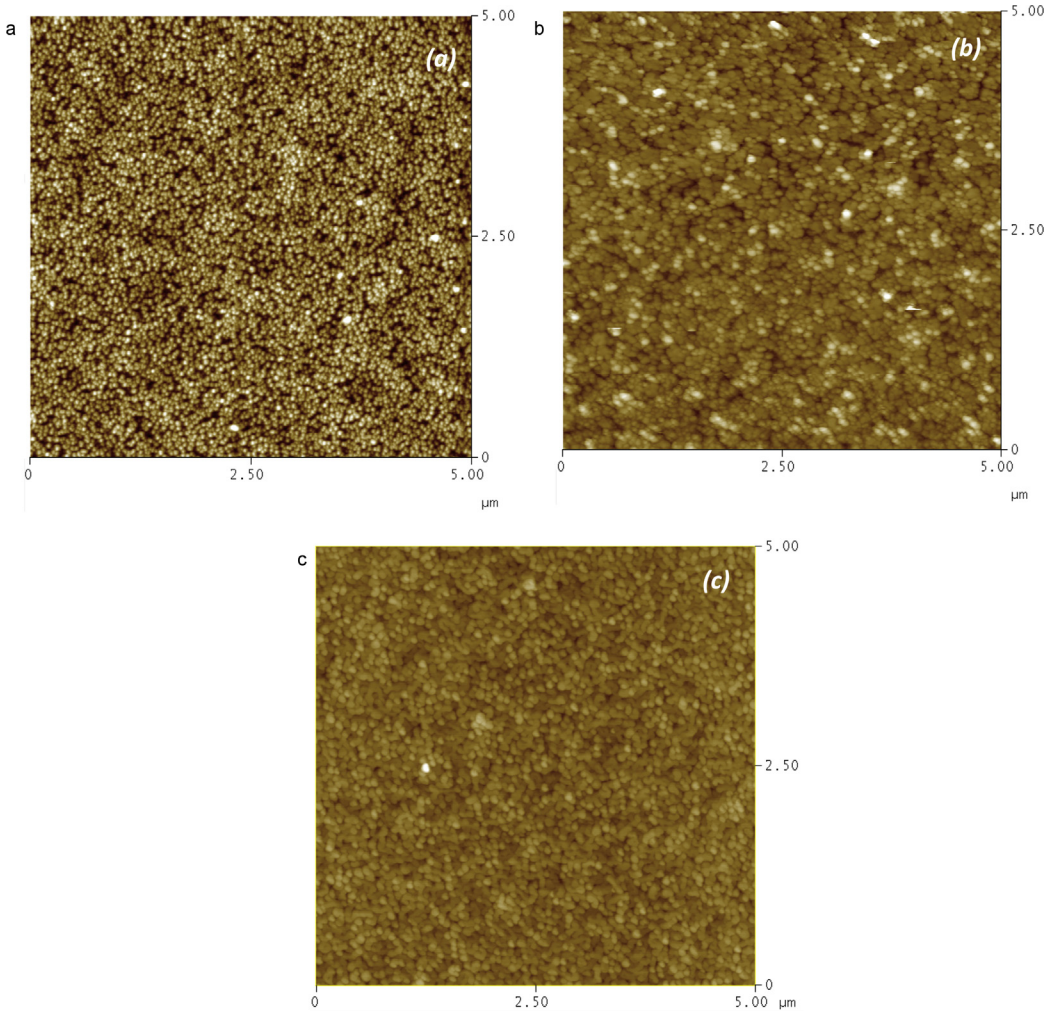

Fig. 3. AFM images of the surface morphology: (a) a LNO thin film on a LAO single crystal substrate; (b) a PCST60 thin film on a LNO/LAO multilayer structure; and (c) a PCST60 thin film on a LAO single crystal substrate.

substrate cannot be clearly distinguished from the corresponding spectrum because the strongest signal from the LAO(1 0 0) single crystal substrate overwhelms the signal from the PCST60 film. The intense Raman peaks at 127, 154 and 487 cm^{-1} in the PCST60/LAO spectrum are due to the LAO(1 0 0) substrate only and can be assigned to optical phonon modes of A_{1g}, E_{1g} and E_{1g} symmetry, respectively [26]. On the other hand, peaks at 283, 301, 459, 524 and 575 cm^{-1} in the PCST60/LAO spectrum are due to the PCST60 tetragonal ferroelectric perovskite phase only (see Fig. 2(a)).

Fig. 2(b) shows unpolarized Raman spectra of PCST60 film grown by LNO/LAO multilayer architecture. In these spectra, the active optical Raman mode signal from the LAO(1 0 0) substrate is absent from spectra which verifies that 360 nm LNO conducting metallic oxide films and the 260 nm PCST60 film are thick enough to effectively eliminate/reduce the optical Raman signal from the LAO(1 0 0) single crystal substrate. In addition, first-order active optical Raman modes at 124, 187, 279, 285, 466, 521, 568 and 735 cm^{-1} were observed which are due to the PCST60 film tetragonal ferroelectric perovskite phase only. Phonon assignments for each mode are A1(1TO), E(2TO), B1 + E, A1(2TO), A1(2LO), E(3TO), A1(3TO), E(3LO) + A1(3LO), respectively, which is supported in the literature [27,28]. Moreover, in the PCST60/LNO/LAO multilayer architecture, a peak at around 401 cm^{-1} could be due to a LNO conductive metallic oxide layer assigned to phonon modes of E_g symmetry [29].

PCST60 and LNO thin film morphology was also investigated by AFM, and the results are displayed in Fig. 3. All these samples exhibited a dense and uniform microstructure with spherical-shaped grains. The LNO oxide film surface on LAO(1 0 0) single crystal substrate is very smooth with an average surface roughness of 6 nm and a grain size of approximately 50 nm. At the same time, the average grain size and root-mean-square roughness values of PCST60 films on LNO/LAO multilayer architecture were approximately 60 nm and 7 nm, respectively. In addition, PCST60 thin films deposited directly on LAO(1 0 0) single crystal substrate have a smoother surface and a grain size slightly larger than the grain size of films deposited on LNO conductive metallic oxide film. These observations can be attributed to different interaction strengths among the LAO single crystal substrate surface, the LNO oxide film and PCST60 thin films which directly influences the nucleation and grain growth mechanism. Average grain size and root-mean-square roughness values for PCST60 thin films directly on LAO(1 0 0) single crystal substrate were 75 nm and 3 nm, respectively.

Cross-sectional measurements reveal that the LNO conductive metallic oxide layer on LAO(1 0 0) single crystal substrate is about 360 nm in thickness whereas PCST60 thin films deposited on LNO/LAO multilayer architecture and directly on LAO(1 0 0) single crystal substrate are about 260 and 340 nm thick, respectively (see Fig. 4(a) and (b)).

Fig. 5(a) shows optical transmittance spectra in the wavelength range of 200–1000 nm from the pure LAO(1 0 0) single crystal substrate and 340 nm thick PCST60 thin films deposited on LAO(1 0 0) single crystal substrate. The PCST60 thin film deposited on LAO(1 0 0) substrate was highly transparent in the infrared region (near infrared NIR 700–1000 nm). The film optical band gap can be determined from the sharply falling transmission region. The low-wavelength absorption data for PCST60 film deposited on LAO(1 0 0) single crystal substrates is related to the fundamental absorption which assumes a transition between the valence and the conduction band. The optical band gap E_g of the PCST60 thin film was determined in the high absorption region by using the Tauc's relation described as [30,31]:

$$(\alpha h\nu)^m = A(h\nu - E_g) \quad (1)$$

where m is a value which characterizes different types of transition (m = 2, 1/2, 2/3 or 1/3 for allowed direct, allowed indirect, forbidden direct and forbidden indirect electronic transitions, respectively), h is the Planck constant, ν is the photon frequency, $h\nu$ is the incident photon energy, α is the absorption coefficient, A is a constant and E_g is the optical band gap value. Absorption coefficients were calculated using the relationship $\alpha = (1/t)\ln(1/T)$, where t is the thickness and T is the transmittance of the PCST60 film. Thus, the dependence of $(\alpha h\nu)^m$ versus incident photon energy ($h\nu$) yields the Tauc optical band gap E_g value. As depicted in Fig. 5(b) and (c), the relationship between $(\alpha h\nu)^2$ and $(\alpha h\nu)^{1/2}$ plotted against ($h\nu$) varies linearly in the high energy region of the absorption edge. Based on the above process, optical band gap E_g values were estimated by extrapolating the linear portion of the plot relating $(\alpha h\nu)^2$ and $(\alpha h\nu)^{1/2}$ versus ($h\nu$) to $(\alpha h\nu)^2 = 0$ and $(\alpha h\nu)^{1/2} = 0$ and considering the direct and indirect nature of the transition process to be 3.56 and 2.87 eV, respectively. Optical band gap values obtained here are similar to results for many wide-band gap semiconductor perovskite structures; i.e., the reported values for the PCT optical band gap are in the 3.56–3.10 eV range depending on the Pb/Ca ratio [32,33].

Fig. 6 shows the frequency dependence of the dielectric constant and dielectric loss of the PCST60 thin film with a configuration of Au/PCST60/LNO/LAO multilayer architecture at room temperature. The dielectric constant shows a slight decrease, and the dielectric loss slowly increases with an increase in frequency which possibly is due to dielectric relaxation which is phenomenon common to major ferroelectric thin films. The PCST60 thin film dielectric constant can rise to 1200 at a frequency of 1 kHz, this value is higher than values for randomly oriented PCST60 thin films on platinum bottom electrodes (around 690 at a frequency of 1 kHz, not

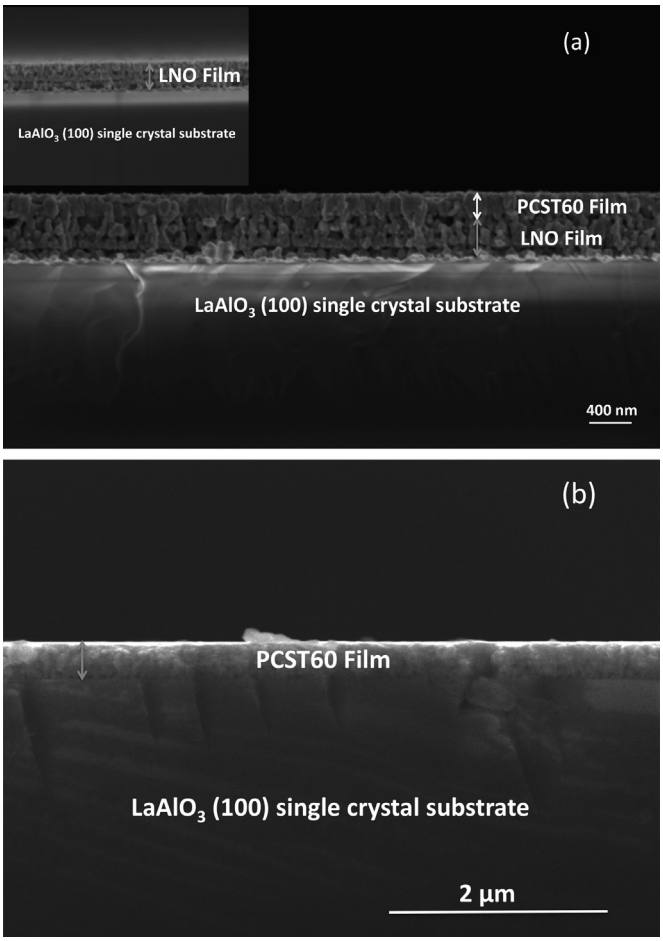

Fig. 4. Cross-sectional FE-SEM micrographs: (a) a PCST60/LNO/LAO multilayer structure; and (b) a PCST60/LAO film. The inset in the (a) shows the LNO layer.

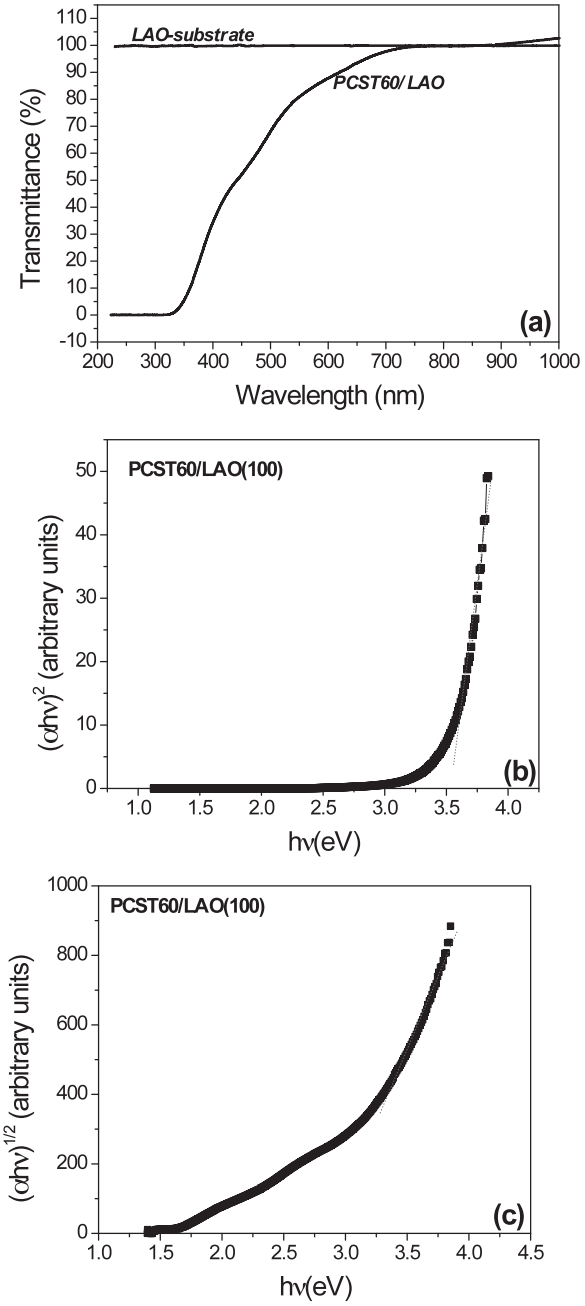

Fig. 5. Optical transmission spectra: (a) a pure LAO(1 0 0) single crystal substrate and a PCST60/LAO structure; (b) $(h\nu\alpha)^2$ versus $h\nu$ plots; and (c) $(h\nu\alpha)^{1/2}$ versus $h\nu$ plots of PCST60/LAO showing optical band gaps.

shown here). This enhancement of the dielectric constant could be attributed to the PCST60 films with higher extent of texture, a dense and uniform microstructure, and it is believed to exist a good lattice matching between LNO layer and the ferroelectric thin film. Such a combination effectively increases the dielectric constant.

PCST60/LNO/LAO structure exhibit ferroelectric characteristics as can be seen from the electric field dependence of the dielectric constant and dielectric loss at a frequency of 100 kHz (see Fig. 7). The butterfly shape exhibited by the PCST60 clearly establishes its ferroelectric nature at room temperature.

PCST60 films exhibit switchable ferroelectric properties prepared on a PCST60/LNO/LAO structure under an applied voltage of 10 V (see Fig. 8) and corroborate the result of the electric field dependence of the dielectric constant in Fig. 7. The PCST60 thin film

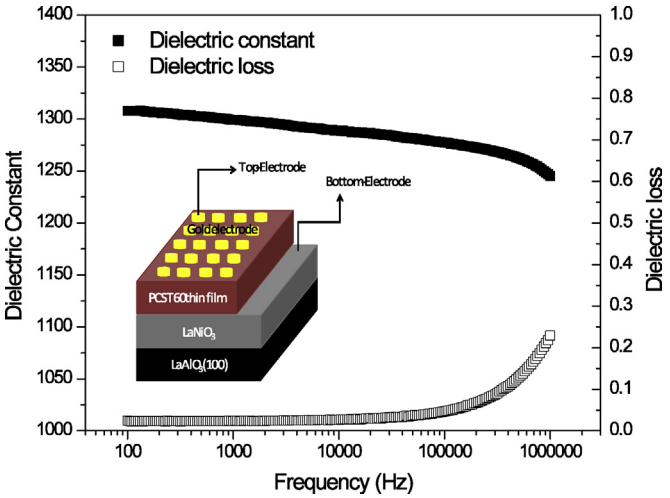

Fig. 6. Frequency dependence of the dielectric constant and dielectric loss of aPCST60 thin film with a Au/PCST60/LNO/LAO configuration. Test devices are schematically drawn in the inset.

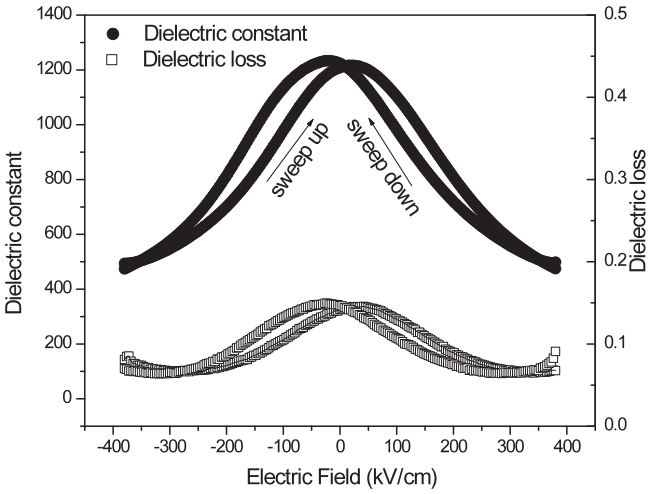

Fig. 7. Dielectric constant and dielectric loss of the Au/PCST60/LNO/LAO multilayer structure as functions of the electric field.

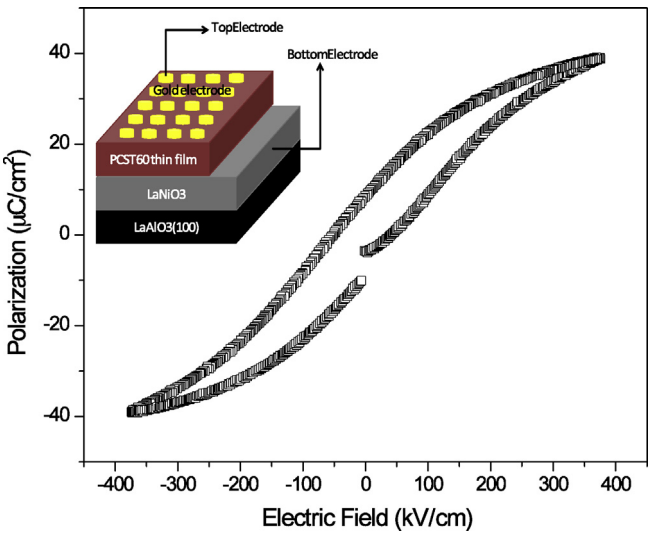

Fig. 8. Polarization–electric field (P–E) hysteresis loop for a Au/PCST60/LNO/LAO multilayer structure. Test devices are schematically drawn in the inset.

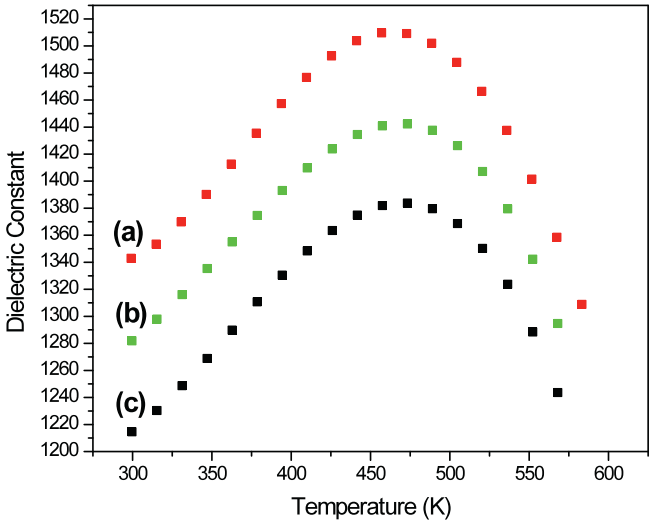

Fig. 9. Temperature and frequency dependence of dielectric constant for a Au/PCST60/LNO/LAO multilayer structure; (a) 1 kHz, (b) 10 kHz and (c) 100 kHz.

showed that the remnant polarization and coercive field are about 12 μC/cm^2 and 46 kV/cm under an electric field around 370 kV/cm, respectively.

Fig. 9 also shows the dielectric constant temperature dependence of a PCST60/LNO/LAO multilayer structure at different frequencies and at 1 kHz, 10 kHz and 100 kHz. Fig. 9 also shows that the dielectric constant value increases gradually to a maximum value as the temperature rises closer to the ferroelectric-to-paraelectric phase transition temperature and thereafter decreasing which indicates a structural phase transition. For PCST60 thin films, the dielectric constant maximum and the corresponding temperature maximum are independent of the measured frequency range. This particular property is typical of ferroelectric classical phase transition. At 1 kHz, 10 kHz and 100 kHz, the ferroelectric-to-paraelectric phase transition temperature was approximately 463 K. In addition, for a normal ferroelectric, in the vicinity of the phase transition temperature, the dielectric stiffness $(1/\varepsilon)$, follows the Curie–Weiss law [34]:

$$\varepsilon = \frac{C}{T - T_0} \tag{2}$$

where C is the Curie–Weiss constant and T_0 is the Curie–Weiss temperature. When T_0 is lower than T_C (phase transition temperature), we observe a first order transition; on the other hand, when $T_0 = T_C$, a second order transition is observed. The parameters C and T_0 were fitted in a narrow temperature range near T_C, at 100 kHz. The best fitting parameters are $C = 3.18 \times 10^5$ K and $T_0 = 413$ K, respectively. The Curie–Weiss temperature for thin film is lower than the transition temperature, as expected from the first order phase transition between the paraelectric and ferroelectric phases.

4. Conclusions

Results clearly revealed the significant impact of highly (1 0 0)-oriented PCST60/LNO/LAO structure on structural and ferroelectric properties prepared by a wet soft chemical method and annealed in a tube oven at 650 °C in an oxygen atmosphere. PCST60/LNO/LAO structure reveals good polarization and dielectric properties resulting from factors such as better extent orientation, a homogenous and dense microstructure. The dielectric constant is above 1200 and is a very attractive candidate for many applications. In addition, following points are viable: (i) the tetragonal perovskite phase was confirmed by unpolarized Raman spectroscopy analysis; (ii) the (1 0 0)-oriented PCST60/LNO/LAO structure exhibit ferroelectric characteristics with a remanent polarization and coercive field of 12 μC/cm^2 and 46 kV/cm, respectively; (iii) the transmittance curve of (1 0 0)-oriented PCST60/LAO(1 0 0) structure had an optical band gap of 3.56 and 2.87 eV for the direct and indirect transition process, respectively; (iv) a diffuse type ferroelectric-to-paralectric phase transition was observed. It is clear that the ferroelectric phase transition is not a relaxor-type transition as the phase-transition temperature is independent of the frequency.

Acknowledgments

This study was financially supported by the Brazilian agencies FAPESP and CNPq. We thank CEPID/CMDMC/INCTMN/CDMF. FAPESP process no. 08/57150-6 and no. 11/20536-7 and CNPq process no. 470147/2012-1.

References

[1] J. Liao, X. Wei, Z. Xu, X. Wei, P. Wang, Mater. Chem. Phys. 135 (2012) 1030.
[2] C. Fu, Z. Huang, J. Li, D. Guo, J. Electron. Mater. 39 (2010) 258.
[3] A. Bhardwaj, N.V. Burbure, G.S. Rohrer, J. Am. Ceram. Soc. 93 (2010) 4129.
[4] Z. Feng, D. Shi, S. Dou, Solid State Commun. 151 (2011) 123.
[5] S. Song, J. Zhai, X. Yao, Mater. Sci. Eng. B 145 (2007) 28.
[6] Y.T. Liu, S.J. Chiu, H.Y. Lee, S.Y. Chen, Surf. Coat. Technol. 206 (2011) 1666.
[7] J. Ge, X. Dong, Y. Chen, F. Cao, G. Wang, Appl. Phys. Lett. 102 (2013) 142905.
[8] Z.H. Tang, M.H. Tang, X.S. Lv, H.Q. Cai, Y.G. Xiao, C.P. Cheng, Y.C. Zhou, J. He, J. Appl. Phys. 113 (2013) 164106.
[9] X.Y. Wen, J. Yu, Y.B. Wang, W.L. Zhou, J.X. Gao, J. Appl. Phys. 108 (2010) 114103–114107.
[10] S.A.S. Rodrigues, J.P.B. Silva, A. Khodorov, J. Martin-Sánches, M. Pereira, M.J.M. Gomes, Mater. Sci. Eng. B 178 (2013) 1224.
[11] A.S. Sidorkina, L.P. Nesterenkoa, A.Yu. Pakhomov, Phys. Solid State 54 (2012) 1008.
[12] A.S. Sidorkin, L.P. Nesterenko, A.L. Smirnov, G.L. Smirnov, S.V. Ryabtsev, Ferroelectrics 349 (2007) 171.
[13] S.J. Chiu, Y.T. Liu, G.P. Yu, H.Y. Lee, J.H. Huang, J. Cryst. Growth 368 (2013) 1.
[14] R. Bouregba, N. Sama, C. Soyer, D. Remiens, J. Appl. Phys. 106 (2009) 044101.
[15] A.Y. Dobin, K.R. Nikolaev, I.N. Krivorotov, R.M. Wentzcovitch, E.D. Dahlberg, A.M. Goldman, Phys. Rev. B 68 (2003) 113408.
[16] Y. Guo, D. Akai, K. Sawada, M. Ishida, Solid State Commun. 145 (2008) 413.
[17] H. Han, J. Zhong, S. Kotru, P. Padmini, X.Y. Song, R.K. Pandey, H. Han, Appl. Phys. Lett. 88 (2006) 092902.
[18] M.S. Awan, A.S. Bhatti, S. Qing, C.K. Ong, Vacuum 85 (2010) 55.
[19] F.M. Pontes, E.R. Leite, G.P. Mambrini, M.T. Escote, E. Longo, J.A. Varela, Appl. Phys. Lett. 84 (2004) 248.
[20] J. Jiang, S.G. Hur, S.G. Yoon, Int. J. Appl. Ceram. Technol. 8 (2011) 1393.
[21] S. Takahara, A. Morimoto, T. Kawae, M. Kumeda, S. Yamada, S. Ohtsubo, Y. Yonezawa, Thin Solid Films 516 (2008) 8393.
[22] H.F. Cheng, Y.C. Chen, C.C. Chou, K.C. Chang, C.S. Hou, I.N. Lin, J. Appl. Phys. 87 (2000) 8695.
[23] M.T. Escote, F.M. Pontes, E.R. Leite, J.A. Varela, R.F. Jardim, E. Longo, Thin Solid Films 445 (2003) 54.
[24] G.H. Aydogdu, S.D. Ha, B. Viswanath, S. Ramanathan, J. Appl. Phys. 109 (2011) 124110.
[25] D. Taylor, Trans. J. Br. Ceram. Soc. 84 (1985) 181.
[26] V.I. Merkulov, J.R. Fox, H.C. Li, W. Si, A.A. Sirenko, X.X. Xi, Appl. Phys. Lett. 72 (1998) 3291.
[27] Y.I. Yuzyuk, Phys. Solid State 54 (2012) 1026.
[28] D.S.L. Pontes, E. Longo, F.M. Pontes, M.A. Pereira-da-Silva, J.H.D. da Silva, A.J. Chiquito, P.S. Pizani, J. Sol–Gel Sci. Technol. 55 (2010) 151.
[29] N. Chaban, M. Weber, S. Pignard, J. Kreisel, Appl. Phys. Lett. 97 (2010) 031915.
[30] J. Yang, T. Zhang, M. Ni, L. Ding, W.F. Zhang, Appl. Surf. Sci. 256 (2009) 17.
[31] M. Bousquet, J.R. Duclère, E. Orhan, A. Boulle, C. Bachelet, C. Champeaux, J. Appl. Phys. 107 (2010) 104107.
[32] F.M. Pontes, D.S.L. Pontes, E.R. Leite, E. Longo, E.M.S. Santos, S. Mergulhão, J.A. Varela, J. Sol–Gel Sci. Technol. 27 (2003) 137.
[33] X.G. Tang, Q.F. Zhou, J.X. Zhang, Thin Solid Films 375 (2000) 159.
[34] M.E. Lines, A.M. Glass, Principles and Applications of Ferroelectrics and Related Materials, Claredon Press, Oxford, 1977, pp. 24.